

Dental microfracture detection using wavelet features and machine learning

Jared Vicory^a, Ramraj Chandradevan^a, Pablo Hernandez-Cerdan^a, Dani Fox^b, Laith Abu Qdais^c, Matthew McCormick^a, Andre Mol^b, Rick Walters^b, Hassem Geha^c, Asma Khan^c, and Beatriz Paniagua^a

^aKitware Inc, Carrboro NC 27510, USA

^bUniversity of North Carolina School of Dentistry, Chapel Hill, NC, 27599, USA

^cUniversity of Texas in San Antonio, School of Dentistry UT Health San Antonio, TX, 78229, USA

ABSTRACT

Microfractures (cracks) are the third most common cause of tooth loss in industrialized countries. If they are not detected early, they continue to progress until the tooth is lost. Cone beam computed tomography (CBCT) has been used to detect microfractures, but has had very limited success. We propose an algorithm to detect cracked teeth that pairs high resolution (hr) CBCT scans with advanced image analysis and machine learning. First, microfractures were simulated in extracted human teeth ($n=22$). hr-CBCT and microCT scans of the fractured and control teeth ($n=14$) were obtained. Wavelet pyramid construction was used to generate a phase image of the Fourier transformed scan which were fed to a U-Net deep learning architecture that localizes the orientation and extent of the crack which yields slice-wise probability maps that indicate the presence of microfractures. We then examine the ratio of high-probability voxels to total tooth volume to determine the likelihood of cracks per tooth. In microCT and hr-CBCT scans, fractured teeth have higher numbers of such voxels compared to control teeth. The proposed analytical framework provides a novel way to quantify the structural breakdown of teeth, that was not possible before. Future work will expand our machine learning framework to 3D volumes, improve our feature extraction in hr-CBCT and clinically validate this model. Early detection of microfractures will lead to more appropriate treatment and longer tooth retention.

Keywords: Isotropic wavelets, Cracked teeth, Deep learning.

1. INTRODUCTION

Epidemiologic studies report that cracked teeth are the third most common cause for tooth loss in industrialized countries, after caries and periodontal disease.¹ This trend is expected to continue to increase as the US population ages² and retain their teeth longer. Recently reported data also shows that cracked teeth are more common in under-served populations.³ Histological studies demonstrate that all cracks are colonized by bacteria, which can cause pulpal and periapical disease,^{4,5} both of which cause intense pain which is the most common reason why patients seek emergency dental care.^{7,6} If left undetected, cracks continue to progress and ultimately result in tooth loss.

Cracked teeth are extremely hard to detect. The clinical symptoms, such as pain upon biting and sensitivity,^{7,7} are often discontinuous with periods of remission. 2D intraoral radiographs and CBCT scans are imaging tools used to detect cracks but also have significant limitations. Radiographs are often insufficient to detect non-displaced cracked teeth because (1) when cracks are not aligned with the x-ray beam they do not result in feature contrast and (2) superimposition of overlying structures and the 3D nature of the cracks limits contrast and hampers interpretation. CBCT adds the advantage of capturing 3D structures but is subject to partial volume effects. Even with the recent developments that offer small Field of View (FOV), high resolution modes

Further author information: (Send correspondence to B.P.)
B.P.: E-mail: beatriz.paniagua@kitware.com

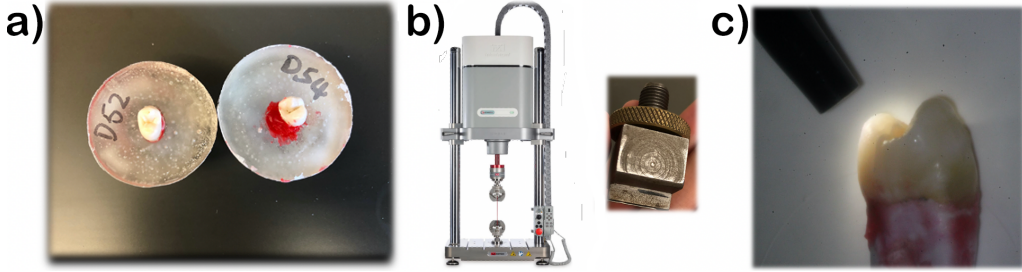


Figure 1. Simulation of fractures in ex-vivo teeth: (left) Preparation of extracted teeth in resin trays; (center) Instron machine and custom insert that simulates intraoral occlusal forces; (right) Confirmation of superficial cracks via transillumination

for endodontic use in CBCT, challenges still exist for the detection of cracks such as those arising from qualitative and subjective human evaluation.^{8,9}

These motivations drove the development of the work presented here, in which we invented an algorithm to provide an enhanced detection and visualization approach by coupling hr-CBCT with advanced image analysis methods and machine learning. Early detection and localization of cracks in a non-invasive, data-driven, quantitative way is of utmost importance in ensuring appropriate treatment and in preventing tooth loss.¹⁰

2. DATA

2.1 Fracture simulation

Our ex-vivo sample consists of 36 extracted human premolars, first molars and second molars. We simulated stress microfractures in a subsample of the total ($n=22$), while the other sound teeth were used as controls ($n=14$). In order to simulate microfractures, the teeth were placed in resin trays and stabilized using dental wax to simulate the periodontal ligament (figure 1.a.).

A customized compression insert was fit into the central grooves of the teeth to evenly distribute forces onto the occlusal surfaces just as would happen in the mouth (1.b.). A continuous force ($\leq 400\text{N}$) was exerted on the grooves using an INSTRON E3000 Electropuls. All the teeth were then examined with and without transillumination by two masked investigators (1.c.). The presence/absence of superficial micro cracks, their location, extent and orientation was recorded. Before image analysis, we confirmed that our standardized method induces cracks in extracted teeth in a reliable manner ($p=0.017$) via Chi square. From that superficial evaluation, cracks are mesio-distally oriented and propagate from the crown towards the root of the tooth, which mimics the common clinical presentations of stress induced dental cracks.

2.2 Micro CT

All teeth were scanned using a desktop microCT imaging system (Bruker Skyscan 1172, Belgium) at a pixel size of $11.97 \mu\text{m}$, with an exposure set at 1500 ms and voltage at 60 kV, $167 \mu\text{A}$, equipped with a 0.5mm Al filter. Scan settings were set at a 0.30 rotation step with a frame averaging value of 8. Reconstruction was performed with a minimum compressed-sensing (CS) value of 0.00000 and maximum CS value of 0.142390.

2.3 High-resolution CBCT

To increase the similarities with its clinical presentation, the teeth were placed in a human jaw and stabilized with wax (figure 2.a). The teeth were randomly arranged so that each jaw contained 2 molars and 1 premolar, and each set of teeth had 2 fractures and 1 control. The jaws were placed in water to mimic soft tissue (figure 2.b). All hr-CBCT volumes were acquired with the Planmeca ProMax 3D Mid ProFace, located at the Oral and Maxillofacial Radiology Clinic at the University of Texas Health San Antonio with acquisition parameters FOV $40 \times 50 \text{ mm}$, 90 kV, 12.5 mA, 15 s, endodontic resolution mode, $75 \mu\text{m}$ voxels.

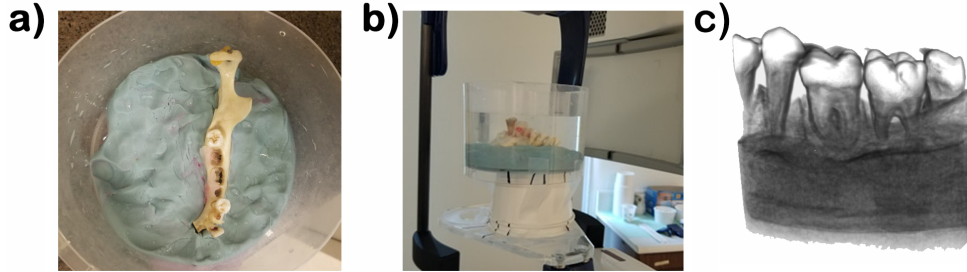


Figure 2. High-resolution CBCT acquisition of our ex-vivo simulated data. a) Dry mandible without teeth placement; b) Acquisition set up; c) Volume rendering of present geometry in scan.

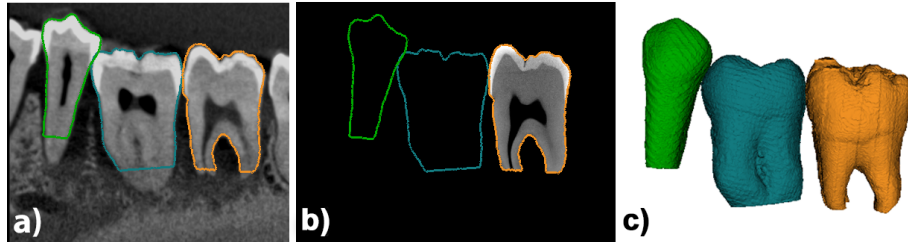


Figure 3. Imaging modalities for ex-vivo data. a) hr-CBCT; b) registered microCT ; c) registered microCT geometry.

3. METHODS

Our method computes imaging features specific to tooth microfractures based on advanced image processing methods and 3D wavelets. These features are then used to train and run a U-Net to enhance the detection of those lesions in teeth.

3.1 Registration and Segmentation of ex-vivo sample

In order to facilitate the detection of fractures in CBCT, we registered the microCT volumes to the CBCT data using the external geometry of the tooth. First, the microCT tooth was segmented using the Otsu method¹¹ followed by an opening operation and a fill holes filter to segment the whole tooth (pulp, dentin and enamel). The geometry in the CBCT was obtained from a fixed threshold (see figure 2.c). The microCT (figure 3.d) was first aligned to the CBCT by a known amount that is custom to pre, first or second molars and refined via the Closest Point algorithm¹² to register the microCT volume and segmentation into the CBCT space (see figure 3.a).

3.2 Feature computation

Our feature extraction pipeline (figure 4.a) includes the following steps: image pre-processing, computation of wavelet pyramid based on the signal present in the input image, monogenic signal generation, phase analysis, and inverse wavelet pyramid construction (spatial reconstruction).

3.2.1 Image pre-processing

Each tooth is cropped from the scan by computing the smallest bounding box that includes the whole tooth geometry. This volume is then padded until all dimensions are multiples of 256 in order to facilitate the wavelet decomposition so different spatial bands do not overlap.

3.2.2 3D Isotropic Wavelets

Wavelets provide a signal decomposition framework that allows for good localization in both the spatial and frequency domains. There is an abundant amount of theoretical work in this field¹³⁻¹⁵ that has been applied to research in areas such as theoretical physics, seismology and image processing. Wavelets are similar to a windowed Fourier Transform, but with the advantage that the spatial resolution can be modulated, localizing imaging features based on both their frequency and location in space.

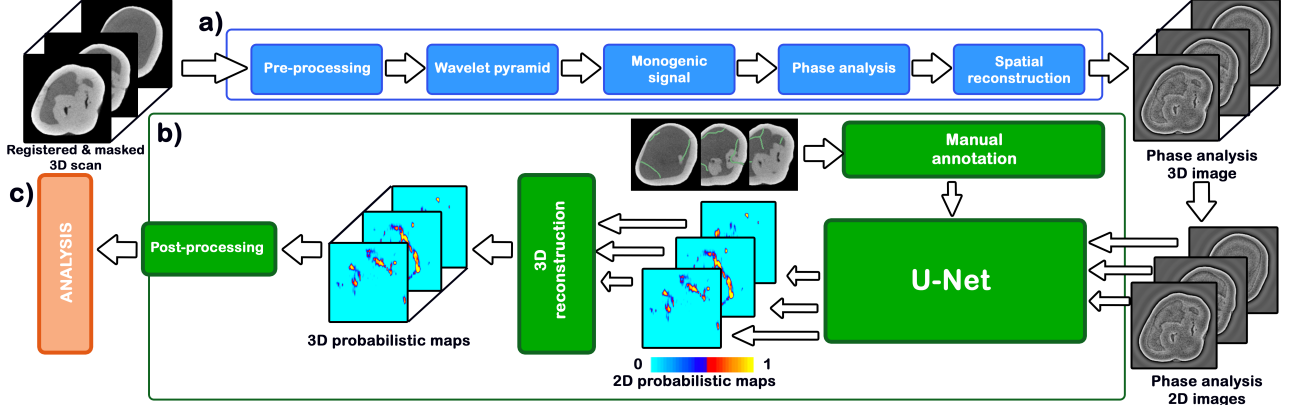


Figure 4. Algorithm workflow. (a) Feature computation, in blue (b) Fracture detection, in green (c) Analytical assessment, in red.

Wavelet decomposition Consider the following wavelet decomposition for a signal f , $\forall f \in L_2(\mathbb{R}^d)$, where s represents the number of levels and l represents the number of high-pass bands.

$$f(x) = \sum_{s \in \mathbb{Z}} \sum_{l \in \mathbb{Z}^d} \langle f, \psi_{s,l} \rangle \psi_{s,l}(x) \quad (1)$$

The family of functions $\{\psi_{s,l}\}$ is a wavelet *frame* (equation 2), constructed by means of *translations* and *dilations* of the *mother wavelet* function ψ .

$$\psi_{s,l}(x) = a^{-d \cdot s / 2} \psi(a^s x - l) \quad (2)$$

Each dilation, defined by the dilation matrix A , squeezes or stretches the mother wavelet, acting as a change of scale. In equation (2) we consider $A = a\mathcal{I}_d$ to be a diagonal matrix with the same dilation factor a in all dimensions. The translation operator l moves and centers the location of the mother wavelet ψ , which must have finite energy $\psi \in L_2(\mathbb{R}^d)$, i.e. $\int_{-\infty}^{\infty} \psi(x)^2 dx < \infty$.

Wavelet pyramid In image processing, the practical implementation of the wavelet transform is called wavelet pyramid construction.^{16–18} This involves passing an image through successive levels of filters where at each level the image is down-sampled and multiple non-overlapping band-pass filters are applied to capture different ranges of frequency components of the input image. Figure 5.a. shows the model of the wavelet pyramid construction process. **By changing the number of high-pass bands, we can capture wide range of frequencies responsible for smooth and sharp edges. By changing the number of levels, we can generate multi-scale versions of an image, where certain scales can capture specific imaging features better than others.** The ultimate result of the wavelet pyramid is a set of wavelet coefficients (in figure 5, see $d_{s,h}$, where $s \in \{1, \dots, \text{Levels}\}$, and $h \in \{1, \dots, \text{HighPassSubBands}\}$).

The forward wavelet pyramid outputs a set of wavelet coefficients with information about each scale. A steerable filter^{16, 18, 19} can be applied to select the orientation where the feature of interest is maximum. We use the Simoncelli steerable filter with 3 scales and 3 high-pass filters.

Monogenic signal and Phase analysis The monogenic wavelet²⁰ is an n-D generalization of the 1-D analytical wavelet signal.²¹ Instead of using the Hilbert transform to convolve the wavelet coefficients, it uses the Riesz transform to generalize the computation to higher dimensions and thus it is well suited for image analysis. The monogenic signal allows for the decomposition of multidimensional signals $f \in L_2(\mathbb{R}^d)$ into phase and amplitude. We can define the monogenic signal as the $d + 1$ dimensional vector

$$f_m(x) = (f(x), R_1 f(x), \dots, R_d f(x)) \quad (3)$$

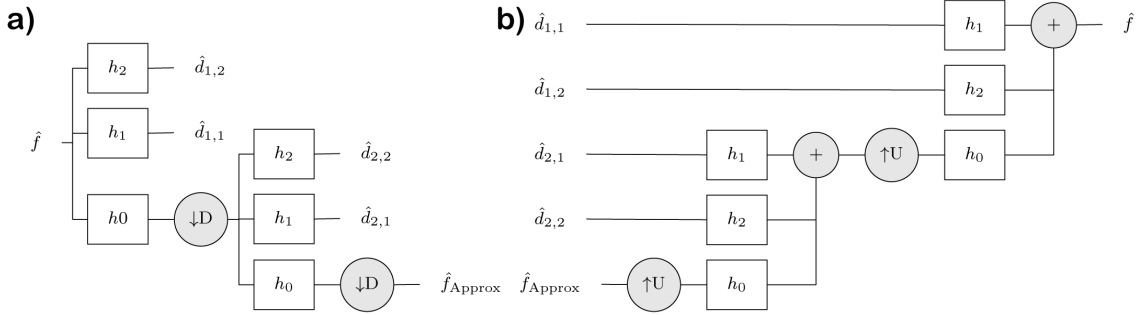


Figure 5. Example of wavelet pyramid for two-level pyramid with two high pass sub-bands. (a) Forward transform: The wavelet coefficients d are the result of applying high-frequency band-pass filters (HP) to the input image in the frequency domain. The process is recursive for the desired number of scales after applying a low-pass frequency filter and a down-sampling operator (D). (b) Inverse transform (spatial reconstruction)

Where R_i denotes the Riesz transform to the dimension i . The phase of the monogenic signal is defined as

$$\alpha_f = \arctan \frac{\sqrt{(R_1 f^2) + \dots (R_d f^2)}}{f} \quad (4)$$

This phase contains information about the signal structure and it is resistant to local image changes in brightness due to artifacts.

Spatial reconstruction The last step is to compute the inverse wavelet pyramid to reconstruct the phase images into the spatial domain (see Figure 5.b). Reconstructing the multiscale coefficients from the phase provides a feature image that enhances microfractures and filaments.

3.3 Fracture detection

The next step consists of using the phase images for the detection of microfractures (figure 4.b) using machine learning. To do this, we use a standard U-Net architecture²² taking 128×128 images as input with 7 convolutional layers and 7 up-sampling layers. The network is trained using a selection of axial slices from 9 each microCT images of teeth with cracks manually annotated.

Because the cracks are so small in volume relative to the size of the image, we start training by dilating the annotations and using a cross entropy loss which is heavily weighted toward reducing false negatives at the expense of the false positive rate. As the network is trained, the annotation dilation is reduced from 7 to 4 to 0 pixels and the cross entropy weighting is moved from weighing false negatives 100× more importantly to weighing them evenly.

The output of the U-Net is an image where each pixel is the probability that a crack is present. For a new 3D volume, we run each axial slice through the network individually and reconstruct a full probability volume. We then threshold this volume at 0.5 and look at connected components remaining in the volume image. In this image, cracks tend to show up as long, thin connected components in the axial slices. Images that have no cracks have fewer, smaller connected components relative to those that have cracks present.

4. RESULTS

Using the technique described in section 3.3 we create images to detect and highlight cracks in images of teeth (Figure 4.c). We look at the number of voxels in the largest connected components of each image as a fraction of the total volume of the image as a measure of likelihood of a crack being present. Computing this measure for 22 images containing cracks and 14 containing no cracks in microCT, we see clear difference between images containing numerous cracks compared with those comparing few or no cracks as shown in Figure 6. In CBCT,

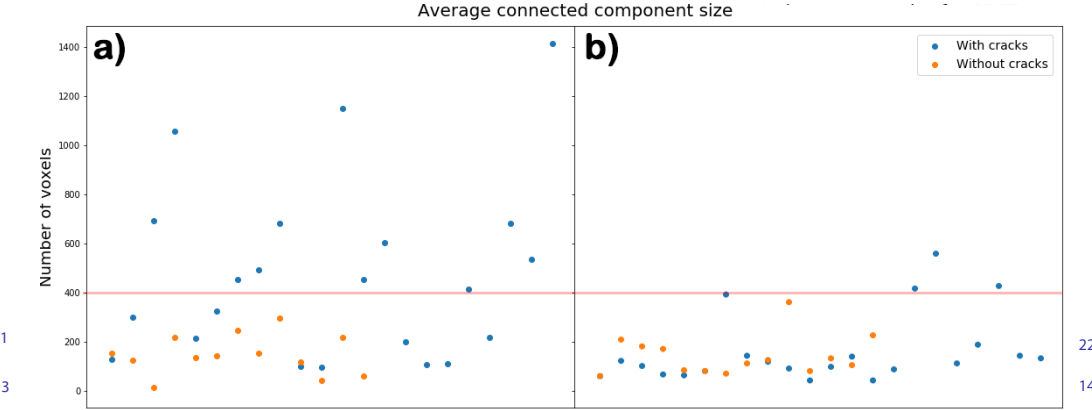


Figure 6. Average connected component size for microCT (left) and CBCT (right) images with (blue) and without (orange) cracks.

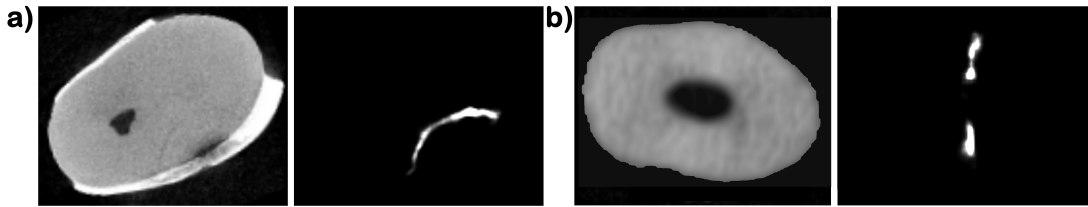


Figure 7. Axial slices of a) a microCT tooth scan with a crack in the lower right and the resulting probability map that highlights the crack; b) a CBCT tooth scan with a spurious detection that can be dismissed due to appearance in the image.

we find that despite of having elevated connected component numbers, there are many more false positives, and thus much more overlap between groups.

Thresholding based on the average size of the 10 largest connected components in each image, we see 13 images with microfractures above a 400 voxel average while no microCT images with no cracks are above this threshold. This measure gives us the ability to flag such images as having a high likelihood of having a crack. In addition, visually inspecting the images and probability maps below this threshold allow the physician to quickly inspect and determine if the highlighted area is a crack or not. Figure 7 shows an example of how the probability maps can guide the physician to the crack.

5. DISCUSSION

We have proposed a method that can enhance the diagnostic accuracy of dental professionals by using the phase images resulting from wavelet analysis to train a deep learning classifier that creates probabilistic maps for microfractures. The proposed wavelet framework presents a superior flexibility and computational performance compared to other methods used for filament-like feature detection, such as the Frangi's vessel enhancement algorithm.²³ This is possible due to the combination of a highly customizable isotropic wavelet backbone that can be configured to be sensitive to features in any orientation and scale.

We are aware that the hr-CBCT currently yields very limited detection ability. Detailed analysis into the acquisition parameters of the hr-CBCT revealed that the endodontic mode often uses smoothing filters intended to provide nice looking images without the presence of artifacts. These filters are useful to better perceive the gross tooth structure and generate 3D reconstructions but can destroy fine features like microfractures. To validate this finding, we tested our algorithm on a previously published dataset of synthetically generated fractures in hr-CBCT.²⁴ Results with this data were similar to microCT, showing that our approach can be applied to CBCT when the images are not over-processed.

Future work will contemplate studying different types of wavelets and classifiers to detect different microfracture types, changing the orientation of the Reisz transform, and validate the algorithm in clinical hr-CBCT images.

ACKNOWLEDGMENTS

Supported by The National Institutes of Health, National Institute of Dental and Craniofacial Research (NIDCR), project R43DE027574.

REFERENCES

- [1] Lynch, C. D. and McConnell, R. J., “The cracked tooth syndrome.,” *Journal (Canadian Dental Association)* **68**, 470–5 (sep 2002).
- [2] Hilton, T. and Ferracane, J., “Cracked Tooth Registry : National Dental PBRN,” (2013).
- [3] “QuickStats: Percentage of Adults Aged 18–64 Years Who Have Had Problems With Their Teeth, by Race/Ethnicity and Type of Problem — National Health Interview Survey, United States, 2008.”
- [4] Ricucci, D., Siqueira, J. F., Loghin, S., and Berman, L. H., “The Cracked Tooth: Histopathologic and Histobacteriologic Aspects,” *Journal of Endodontics* **41**, 343–352 (mar 2015).
- [5] Kahler, B., Moule, A., and Stenzel, D., “Bacterial contamination of cracks in symptomatic vital teeth.,” *Australian endodontic journal : the journal of the Australian Society of Endodontontology Inc* **26**, 115–8 (dec 2000).
- [6] Iqbal, M., Kim, S., and Yoon, F., “An Investigation Into Differential Diagnosis of Pulp and Periapical Pain: A PennEndo Database Study,” *Journal of Endodontics* **33**, 548–551 (may 2007).
- [7] Rivera, E. M. and Williamson, A., “Diagnosis and treatment planning: cracked tooth.,” *Texas dental journal* **120**, 278–83 (mar 2003).
- [8] Setzer, F. C., Hinckley, N., Kohli, M. R., and Karabucak, B., “A Survey of Cone-beam Computed Tomographic Use among Endodontic Practitioners in the United States,” *Journal of Endodontics* **43**, 699–704 (may 2017).
- [9] Brady, E., Mannocci, F., Brown, J., Wilson, R., and Patel, S., “A comparison of cone beam computed tomography and periapical radiography for the detection of vertical root fractures in nonendodontically treated teeth,” *International Endodontic Journal* **47**, 735–746 (aug 2014).
- [10] Banerji, S., Mehta, S. B., and Millar, B. J., “Cracked tooth syndrome. Part 1: aetiology and diagnosis,” *BDJ* **208**, 459–463 (may 2010).
- [11] Otsu, N., “THRESHOLD SELECTION METHOD FROM GRAY-LEVEL HISTOGRAMS.,” *IEEE Trans Syst Man Cybern SMC-9*(1), 62–66 (1979).
- [12] Zhang, Z., “Iterative point matching for registration of free-form curves and surfaces,” *International Journal of Computer Vision* **13**, 119–152 (oct 1994).
- [13] Mallat, S. G., “A Theory for Multiresolution Signal Decomposition: The Wavelet Representation,” *IEEE Transactions on Pattern Analysis and Machine Intelligence* **11**(7), 674–693 (1989).
- [14] Heil, C. E. and Walnut, D. F., “Continuous and discrete wavelet transforms,” *SIAM Review* **31**, 628–666 (feb 1989).
- [15] Kovesi, P., “Image Features From Phase Congruency,” tech. rep. (1995).
- [16] Held, S., Storath, M., Massopust, P., and Forster, B., “Steerable Wavelet Frames Based on the Riesz Transform,” *IEEE Transactions on Image Processing* **19**, 653–667 (mar 2010).
- [17] Chenouard, N. and Unser, M., “3D Steerable Wavelets in Practice,” *IEEE Transactions on Image Processing* **21**, 4522–4533 (nov 2012).
- [18] Unser, M., Chenouard, N., and Van De Ville, D., “Steerable pyramids and tight wavelet frames in L2(Rd),” *IEEE Transactions on Image Processing* **20**, 2705–2721 (oct 2011).
- [19] Simoncelli, E. P. and Freeman, W. T., “Steerable pyramid: a flexible architecture for multi-scale derivative computation,” in [*IEEE International Conference on Image Processing*], **3**, 444–447, IEEE (1995).
- [20] Felsberg, M. and Sommer, G., “The monogenic signal,” *IEEE Transactions on Signal Processing* **49**(12), 3136–3144 (2001).

- [21] Selesnick, I. W., Baraniuk, R. G., and Kingsbury, N. G., “The dual-tree complex wavelet transform,” (2005).
- [22] Ronneberger, O., Fischer, P., and Brox, T., “U-net: Convolutional networks for biomedical image segmentation,” in [*Lecture Notes in Computer Science (including subseries Lecture Notes in Artificial Intelligence and Lecture Notes in Bioinformatics)*], **9351**, 234–241, Springer Verlag (2015).
- [23] Frangi, A. F., Niessen, W. J., Vincken, K. L., and Viergever, M. A., “Multiscale vessel enhancement filtering,” 130–137, Springer, Berlin, Heidelberg (1998).
- [24] Paniagua, B., Shah, H., Hernandez-Cerdan, P., Budin, F., Chittajallu, D., Walter, R., Mol, A., Khan, A., and Vimort, J.-B., “Automatic quantification framework to detect cracks in teeth,” in [*Medical Imaging 2018: Biomedical Applications in Molecular, Structural, and Functional Imaging*], Gimi, B. and Krol, A., eds., **10578**, 55, SPIE-Intl Soc Optical Eng (mar 2018).